



Detector calibration and measurement issues in multi-color time-resolved laser-induced incandescence

Raphael Mansmann¹ · Timothy A. Sipkens² · Jan Menser¹ · Kyle J. Daun² · Thomas Dreier¹ · Christof Schulz¹

Received: 27 November 2018 / Accepted: 9 June 2019 / Published online: 18 June 2019
© Springer-Verlag GmbH Germany, part of Springer Nature 2019

Abstract

Time-resolved laser-induced incandescence is used to infer the size distribution of gas-borne nanoparticles from time-resolved pyrometric measurements of the particle temperature after pulsed laser heating. The method is highly sensitive to aspects of the measurement strategy that are often not considered by practitioners, which often lead to discrepancies between measurements carried out under nominally identical conditions. This paper therefore presents a well-documented calibration procedure for LII systems and quantifies the uncertainty in pyrometric temperatures introduced by this procedure. Calibration steps include corrections for: (1) signal baseline, (2) variable transmission through optical components, and (3) detector characteristics (i.e., gain and spectral sensitivity). Candidate light sources are assessed for their suitability as a calibration reference and the uncertainty in calculated calibration factors is determined. The error analysis is demonstrated using LII measurements made on a sooting laminar diffusion flame. We present results for temperature traces of laser-heated particles determined using two- and multi-color detection techniques and discuss the temperature differences for various combinations of spectral detection channels. We also summarize measurement artifacts that could bias the LII signal processing and present strategies for error identification and prevention.

1 Introduction

Laser-induced incandescence (LII) is a diagnostic for in situ nanoparticle size and volume fraction measurements of both soot [1–3] and inorganic aerosols [4–12]. The measurement principle is based on pulsed laser heating of gas-borne nanoparticles within a sample volume. At incandescent temperatures (typically higher than 2000 K), the spectral incandescence emitted by the nanoparticles at two or more discrete wavelength bands is used to define an instantaneous effective temperature of the ensemble through pyrometry.

The particle volume fraction can be inferred from the signal intensity, while the temporal variation of the spectral incandescence (and thus particle temperature) yields the nanoparticle size, as small nanoparticles cool more quickly than large ones. Measurements of the decaying incandescence is commonly called time-resolved LII (TiRe-LII) and focuses on the determination of nanoparticle size [7, 13, 14] along with other parameters associated with the heat transfer model. The analysis of TiRe-LII signals is typically split into two major parts: (1) modeling the spectral characteristics, which describes the nanoparticle–light interaction both for absorption and emission, and relates the observed spectral incandescence to the effective temperature, and (2) heat transfer modeling, which uses the effective temperature decay to infer the mean nanoparticle diameter.

Because of the high dynamic range of the signal, its fast temporal variation, and the strong dependence on radiometric evaluations, the LII method is highly sensitive to experimental details and the chosen hardware. Variations of the results reported for measurements under nominally identical conditions are attributed to seemingly minor variations in the experimental approaches. Discussions during the biennial LII workshop series [15–17] revealed that strategies for detector

This article is part of the topical collection “Laser-Induced Incandescence”, guest edited by Klaus Peter Geigle and Stefan Will.

✉ Raphael Mansmann
raphael.mansmann@uni-due.de

¹ Institute for Combustion and Gas Dynamics—Reactive Fluids (IVG), Center for Nanointegration Duisburg-Essen (CENIDE), University of Duisburg-Essen, Duisburg, Germany

² Department of Mechanical and Mechatronics Engineering, University of Waterloo, Waterloo, Canada

calibration/operation and signal processing vary widely and, despite their fundamental importance, these topics are rarely addressed in a rigorous manner. This paper shows that these variations can lead to measurement artifacts that significantly impact how the LII signal is interpreted. We examine the origin of these artifacts, and present strategies for error mitigation.

The incandescence signal is usually measured with fast photomultiplier tubes (PMT) or gated cameras equipped with bandpass filters, gated spectrometers, or streak cameras. The measurement strategy can be classified based on the number of discrete detection wavelength bands, or, in the case of spectrometers and streak cameras, the detection of a nearly continuous spectrum. For single-color TiRe-LII, one PMT equipped with a bandpass filter is used to measure the incandescence decay rate of the laser-heated nanoparticles. This incandescence is compared with simulated incandescence traces generated using a heat transfer model to recover the nanoparticle size. While this approach can be used to make comparative measurements (e.g., how soot primary particle sizes vary within a flame), it is insufficient for absolute size measurements, since the peak nanoparticle temperature needed for this calculation must be inferred from the absorption cross-section and the local gas temperature, which are rarely known with a high degree of certainty.

More accurate results can be obtained by incorporating additional spectral detection bands, which provides a route to calculate the particle temperature directly. While at least two detectors equipped with different bandpass filters [7, 14, 18, 19] are required for this approach, recent work is increasingly considering three or more wavelengths [20, 21] or nearly continuous spectra as measured by a spectrometer coupled to a streak camera [12, 22].

All these approaches require the detectors to be calibrated with respect to their relative spectral sensitivity and to account for issues of linearity, measurement artifacts, and interference from other light sources (particularly within flames). Inadequate calibration practices and poor signal quality can lead to large errors in quantities inferred from LII. This is highlighted by the fact that there are often discrepancies in the temperatures inferred using different channel combinations of two-color LII and that the analysis of the resultant temperature traces from previously published LII models often yields very different particle sizes [21]. Moreover, these errors can be easily misinterpreted as “physical” processes resulting from time-varying thermo-physical properties or increasingly complex spectroscopic and transport phenomena, resulting in the development of faulty measurement models.

This work proceeds by defining the requirements for the detection setup and a summary of measurement artifacts that may affect LII signals. This is followed by an overview of photomultiplier characteristics and a mathematical description of the calibration procedures for PMT sensitivity, PMT

gain, and variable optical components within an LII setup. The LII signal-processing steps and the spectroscopic model used to determine the temperature are described along with their implementation within the Bayesian framework, which provides an estimate of the uncertainty introduced by the calibration procedures and the measurement. The subsequent section gives an overview of the experimental apparatus that is used to evaluate the best-suited calibration strategy. The apparatus consists of four calibration light sources, the LII detection setup and a laminar diffusion flame that is used as a target. The calibration procedures are shown for this setup, and the suitability of various light sources for calibration is evaluated. For the uncertainty analysis, reference measurements are carried out on an ethene-fueled laminar diffusion flame and the temperatures inferred using two-color and multi-color pyrometry are discussed within the context of the Bayesian framework. Additional measurement artifacts that can cause a bias during LII signal acquisition are presented in the supporting materials section.

2 Theory

2.1 Detector requirements and measurement issues in LII

The TiRe-LII detection system should be designed with components selected according to several criteria: (1) absolute and spectral sensitivity; (2) linearity, gain and dynamic range; (3) rise- and fall-time characteristics; (4) reproducibility and drift; and (5) chromatic aberrations of the focusing optics and apertures. Problems with any of these aspects of the detection system will cause measurement errors that bias the signals, their temporal variation and, by extension, the pyrometrically inferred temperature and quantities derived therefrom (e.g., nanoparticle size). Linearity of the detection system ensures that the electronic signal generated by the detector is proportional to the irradiance incident on the detector. While most LII studies presume linearity, nonlinear PMT behavior has been reported in some experiments [23, 24], as well as in other applications like laser-induced luminescence [25] and phosphor thermometry [26]. Nonlinear detector behavior can introduce large errors into the ratio-based pyrometric temperature. This is particularly challenging for LII experiments where the incandescence signal strength varies by several orders of magnitude over a single measurement trace (e.g., five orders of magnitude between 1500 and 4000 K in the visible range). This requires that the detector has a large dynamic range to obtain robust estimates of the aerosol attributes. The detectors can also be gated by temporally disabling the gain circuit, thereby avoiding saturation by background flame radiation or damage caused by strong excitation light (as in the case of double pulse LII [5, 27]). Gated

operation can also be used to block a part of the initial LII signal and increase the dynamic range by a sequential detection of parts of the signal trace with adapted gain settings and ND filters [28]. At the same time, the rise- and fall-time characteristics of the detectors need to be sufficiently fast (<2 ns rise-time) to resolve the rapidly varying LII signal. Slow detector response, either caused by a slow detection technology or built-in low-bandwidth electronic components (e.g., low-bandwidth amplifiers), can falsely suggest larger particle sizes in cases with fast signal decay [29, 30]. To obtain an unbiased pyrometric temperature estimate, multiple detectors (working in different wavelength ranges) must operate reproducibly and must be drift free. Additionally, the detection system must be calibrated for relative spectral sensitivity. Absolute sensitivity calibration is not required for time-resolved LII but is essential for determining the soot volume fraction using the auto-compensating LII technique [14]. The detection system could also include chromatic errors through focusing optics and apertures [31], which can be particularly important when using low *f*-number optics [32]. Will et al. [33] noted that a short-pass filter could still show significant transmission in the near IR, which can cause unexpected interference from background radiation. In summary, it is important to correctly identify common measurement artifacts to distinguish signal bias from effects associated with incandescence from the laser-heated nanoparticles.

2.2 Photomultiplier tubes

Most LII detection systems are based on photomultiplier tubes (PMTs). Accurate calibration and measurements require knowledge of PMTs and which of their components can influence the signal quality. Figure 1 shows a schematic of a PMT, including its three major components: photocathode, electron multiplier, and anode.

In a PMT, the primary emission (photocathode) and secondary emissions (dynodes) of electrons can both be subject to nonlinearity. The photocathode resistivity increases with increasing incident photon flux, which results in the

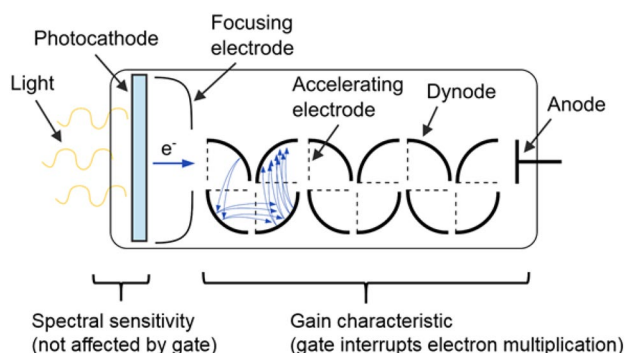


Fig. 1 Schematics of a photomultiplier tube

release of fewer photoelectrons. In other cases, when the electron multiplier gain is too high, space-charge effects at the last dynode stages limit the anode current [34, 35]. The first effect is more likely for semi-transparent photocathodes [34], while the latter effect is most likely to occur at low light levels with high gain [35, 36]. The photon flux during the LII signal peak is usually much higher compared to measurements at lower light levels and nonlinearity has been reported for anode current levels lower than the manufacturer-specified limit [24]. In this context, it was demonstrated that bi-alkali photocathodes (SbKCs) are more prone to nonlinear behavior than multi-alkali (SbNa2KCs) photocathodes [24]. It is important to keep this in mind when using gated PMTs as the electrical gate circuit only interrupts the high-voltage power supply of the dynode stages rather than preventing primary photoelectron emission from the photocathode. Consequently, even when the gate is inactive, the photocathode can be depleted, affecting the linearity of the measurement or calibration.

This study focuses on compact PMT modules with a built-in high-voltage power supply, voltage-divider circuit and gate circuit, which have recently become commercially available. This leaves the experimentalist with three adjustable operating parameters: (1) the incident light flux, via variable neutral density (ND) filters; (2) the electron gain, by changing the control voltage of the voltage-divider circuit; and (3) the gate-opening time and duration. The PMT gain characteristics depend on the number and type of dynode stages, the voltage-divider circuit design, and the applied gain voltage. It can be approximated experimentally by plotting the gain and gain voltage on logarithmic axes [35, 37]. An additional advantage of gated PMTs is that the signal baseline (dark current) can be determined immediately before the gate opening of each individual signal trace; while for ungated operation, the baseline needs to be determined prior to the experiment.

2.3 Calibration procedure

Calibration can be done either directly or indirectly [2, 38]. Indirect approaches calibrate by comparing an LII-inferred aerosol attribute (e.g., particle volume fraction or particle size) against values obtained from an independent measurement techniques, most often extinction measurements [39–43], gravimetric sampling [44, 45], or transmission electron microscopy (TEM) [12, 46]. Indirect approaches may also consider aerosol sources with properties reported in literature [4, 47–49] or those generated by aerosolizing commercially available, pre-characterized powders [4, 50, 51]. In direct calibration, by contrast, the spectral emission is measured from a source of known radiance, and the relative instrument sensitivity is obtained from the ratio of the measured spectrum and the reference spectrum. The relative

sensitivity calibration of the measurement system is essential when determining the pyrometric temperature from the response of two or more detectors. While direct calibration allows the measured signals to be directly related to a physical quantity (i.e., spectral incandescence) that acts as an input for the LII model, indirect approaches simply scale the measured signal to match an expected particle size or volume fraction. As the properties of calibrated aerosols tend to be uncertain (e.g., varying with process condition or time), this results in significant uncertainties in indirect calibration procedures. Therefore, the remaining discussion focuses on the direct calibration procedure.

Typically, direct calibration is carried out by placing a well-characterized light source at the LII probe volume thereby including all of the optical components in the sensitivity calibration. The most common source is the calibrated tungsten filament lamp [14, 20, 31, 52–54], which can be approximated as a gray body at temperatures between 2000 and 4000 K, depending on the lamp current. However, the lamp cannot be modeled as spatially uniform or diffuse (i.e., the emitted intensity varies with angle and location). Consequently, calibration accuracy depends strongly on the ratio of filament size and LII probe volume, and further optical elements (e.g., a pinhole, a diffuser, or an integrating sphere) may be introduced to account for a non-Lambertian intensity distribution. Ryer et al. [55] used an integrating sphere in combination with a halogen lamp to homogenize the intensity distribution. Smallwood [53] used a calibrated spectrometer attached to an integrating sphere to trace the lamp performance and calculate a reference spectrum. Irradiance standards are light-source systems that are calibrated against an independent standard and optimized for homogeneity and reproducibility with various optical elements. Recent studies used irradiance standards with a calibrated tungsten/halogen lamp equipped with a diffuser system [20, 56] or a quartz halogen lamp scattered off the surface of a

Lambertian surface [53]. In contrast, Cenker and Roberts [57] calibrated their detectors for relative sensitivity using incandescence from a well-characterized reference flame. A drawback of this approach is that variations in process conditions could affect the temperature profile of the flame and thus directly affect the calibration. Spectral incandescence at typical flame temperatures (~ 1600 K) is also quite weak at the shorter detection wavelengths typical in most LII measurements.

The following sections demonstrate the optical sensitivity calibration procedures and error calculation for a multi-wavelength LII device. Before the signals from multiple PMTs can be used for LII signal processing, four calibration steps need to be performed to account for: (1) signal baseline, (2) relative channel sensitivity, (3) PMT gain characteristics, and (4) variable optical components (i.e., neutral density (ND) filter, collection optics). Figure 2 shows a schematic of a typical LII setup and indicates the components affected by the individual calibration steps. The following calibration procedures can be applied to any LII system with two or more PMTs.

2.3.1 Baseline correction and signal range

The baseline signal, $V_i^{baseline}$, is related to the PMT signal measured in a dark environment and represents the reference zero line for all subsequent processing steps. The baseline can be nonzero if thermal noise in the PMT produces a dark current or if the oscilloscope offset is nonzero. Baseline drift can occur if the electronics are not in thermal equilibrium with the surrounding (see “Appendix”). The baseline should not be confused with the bias caused by background illumination, e.g., flame radiation along the optical path. For ungated PMTs, the baseline signal level is found using an independent dark measurement, which is later subtracted from the measured signal, while for gated PMTs the signal

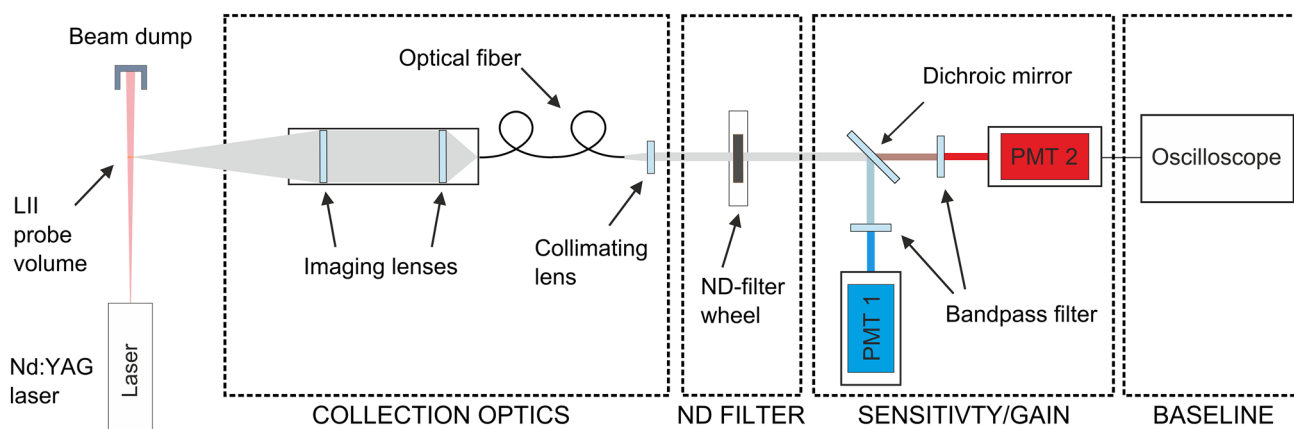


Fig. 2 Schematics of a typical LII setup indicating the components affected by the individual calibrations. The calibration light source is usually placed at the LII probe volume position

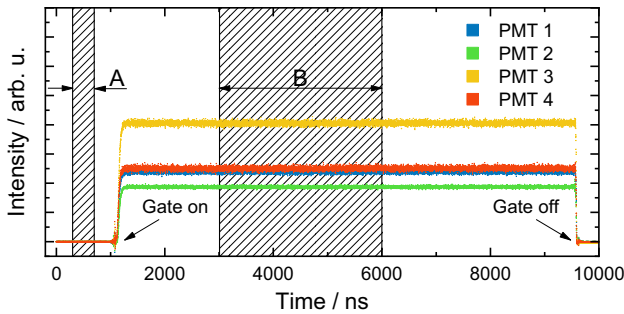


Fig. 3 Signal trace of a gated PMT. Signal sections A and B are used for the calibration procedure

before the gate opening can be used to obtain a mean baseline signal level. Figure 3 illustrates typical signals obtained from four gated PMTs, along with the corresponding signal sections used for various calibration procedures. Section A is used for baseline correction and section B is averaged to calculate a mean signal and its standard deviation from a sufficiently large number of signals (> 100). Section B needs to be sufficiently distant (> 1 μs) from the PMT gating to avoid any biases introduced by the gating characteristics.

2.3.2 Relative PMT sensitivity calibration

In two- or multi-color LII measurement systems, the PMTs must be calibrated relative to one another. For this purpose, the irradiance of a spectrally known light source is measured at constant gain voltage, which defines a reference point, $V_{g,ref}$, that is discussed in Sect. 2.3.3. The PMT signal response of all of the LII channels can then be used to calculate the relative spectral sensitivity of the PMT at this gain voltage. Depending on the light level of the calibration light source or LII signals, it may also be necessary to reduce the light intensity using calibrated ND filters to avoid biases like nonlinearity. The spectral transmittance of the ND filter is usually sufficiently flat over the bandpass filter widths that it can be approximated by a mean transmittance, τ_{ij} , for the i th channel and j th filter. Repeating the sensitivity calibration at various light levels using different ND filters will determine if a PMT and its calibration are affected by nonlinearity [24]. Figure 4 shows a reference spectrum of an integrating sphere light source and the transmission spectra of the bandpass filters used in this study.

Let E_{ik} represent the irradiance detected by the i th sensor due to emission from the k th light source. If the detector is equipped with a bandpass filter with center wavelength $\lambda_{c,i}$ and bandwidth $2\delta_i$, E_{ik} can be calculated by integrating the product of the reference spectral irradiance, $E_k^{ref}(\lambda)$, and the spectral sensitivity of the LII system, $\Theta(\lambda)$, over the spectral width of the bandpass filter

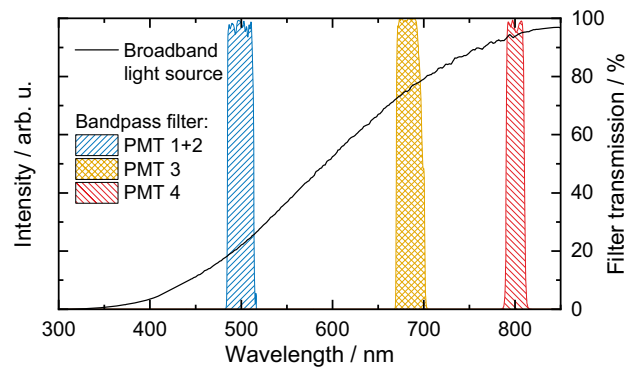


Fig. 4 Reference spectrum of the integrating sphere broadband light source and the

$$E_{ik} = \int_{\lambda_{c,i}-\delta_i}^{\lambda_{c,i}+\delta_i} \Theta(\lambda)E_k^{ref}(\lambda)d\lambda \approx \Theta_i E_{ik}^{ref}. \tag{1}$$

Assuming that the spectral transmittance of the bandpass filter and the spectral sensitivity of the detectors are constant over the narrow filter bandwidth, the spectral sensitivity of the LII system can be approximated at the center wavelengths of the detectors [14, 20], $\Theta_i = \Theta(\lambda_{c,i})$, to give

$$E_{ik} \approx \Theta_i E_{ik}^{ref}, \tag{2}$$

where

$$E_{ik}^{ref} = \int_{\lambda_{c,i}-\delta_i}^{\lambda_{c,i}+\delta_i} E_k^{ref}(\lambda)d\lambda. \tag{3}$$

While this approximation will introduce an additional bias into the measurement, we assume that this bias is small relative to the other biases considered in this work. The irradiance E_{ik} , can be related to the measured PMT voltage with an additional instrument calibration factor η_i that scales the irradiance measured with a detector to a voltage:

$$V_{ik}^{meas} - V_i^{baseline} = \eta_i E_{ik} = \eta_i \Theta_i E_{ik}^{ref}. \tag{4}$$

Knowledge of the exact value of $\eta_i \Theta_i$ is only needed to measure the particle volume fraction and requires an absolute calibrated light source (see Ref. [14]). For light sources that are only calibrated for relative sensitivity, the true value of $\eta_i \Theta_i$ is unknown and a relative sensitivity calibration factor can be defined according to

$$D_i^* \propto \frac{1}{\eta_i \Theta_i}. \tag{5}$$

For the present analysis, the relative sensitivity calibration factor D_{ijk}^* for the i th PMT channel, j th ND filter, and

k th light source is defined from the measured mean signal voltage, the baseline voltage, the ND-filter transmittance, and the reference spectrum:

$$D_{ijk}^* \equiv \frac{\tau_{ij} E_{ik}^{\text{ref}}}{V_{ijk}^{\text{meas}} - V_i^{\text{baseline}}}. \tag{6}$$

As we only consider the relative sensitivity here, calibration sets resulting from measurements with light sources of varying intensity and different ND filters can be compared by scaling the relative sensitivity calibration factors by the mean value for each light source:

$$D_{ijk} = \frac{nm}{\sum_i^m \sum_j^n} D_{ijk}^* \tag{7}$$

In general, the calibration factors can be envisioned as normally distributed random variables due to imperfect knowledge of the reference spectra and variations in measured quantities for which a mean and standard deviation are often known. This results in calibrated LII signals that will also follow a normal distribution. To quantify the uncertainty associated with the calibration factors, the mean, \bar{D}_i , and standard deviation, σ_{D_i} , of D_{ijk} over the various light sources and ND filters are incorporated into a Bayesian approach when processing signals in the following sections.

2.3.3 PMT gain calibration

The gain of a PMT is the ratio of the incident photon flux to the generated anode current, which can be controlled by varying the gain voltage of the high-voltage divider circuit in the PMT. Variation of this quantity increases the dynamic range of PMTs and allows measurements over a wide range of light levels. The anode current is usually measured as a voltage signal using the internal impedance of the oscilloscope (typically 50 Ω). While neutral density filters reduce the light level only by a fixed factor, the gain can be used to increase the PMT signal to match the range of analog-to-digital converter (ADC) voltages measurable by the oscilloscope. This allows users to make full use of the digitization depth, thereby maximizing the signal-to-noise ratio. In cases where PMT measurements are taken at a range of gain voltages, the calibration coefficient of each channel must additionally be multiplied by a gain correction factor.

The mean baseline-corrected anode current, i_i^a , produced by a PMT can be related to the actual gain voltage, V_i^{gain} , in the linear range of the PMT by

$$\ln(i_i^a) = A_i \ln(V_i^{\text{gain}}) + B_i. \tag{8}$$

The coefficient B can be eliminated by normalizing about a reference gain voltage, $V_i^{\text{g,ref}}$, and a corresponding anode current, $i_i^{\text{a,ref}}$,

$$\frac{i_i^a}{i_i^{\text{a,ref}}} = \exp \left[A_i \ln \left(\frac{V_i^{\text{gain}}}{V_i^{\text{g,ref}}} \right) \right] = \left(\frac{V_i^{\text{gain}}}{V_i^{\text{g,ref}}} \right)^{A_i}. \tag{9}$$

This relationship can be rewritten in terms of the gain correction function,

$$G_i(V_i^{\text{gain}}) \equiv \left(V_i^{\text{gain}} / V_i^{\text{g,ref}} \right)^{-A_i}, \tag{10}$$

such that the anode current expected at the reference gain voltage can be calculated from the anode current at any other gain voltage,

$$i_i^{\text{a,ref}} = i_i^a G_i(V_i^{\text{gain}}). \tag{11}$$

The value of A_i can be determined by applying weighted least squares to Eq. (9) using anode currents measured at a range of gain voltages,

$$A_i = \arg \min_A \left\{ \left\| \frac{i_i^a - i_i^{\text{a,ref}} \left(V_i^{\text{gain}} / V_i^{\text{g,ref}} \right)^A}{\sigma_{i_i^a}} \right\|_2^2 \right\}, \tag{12}$$

where $\sigma_{i_i^a}$ is the standard deviation of i_i^a , which can be estimated by making multiple measurements of the anode current. By approximating the problem as locally linear, uncertainties in A_i can be determined using traditional statistical techniques and propagated through to G using the propagation-of-error formula [58]:

$$\sigma_{G_i} = \sigma_A \left| \frac{dG_i}{dA} \right| = \sigma_A \left| - \left(\frac{V_i^{\text{gain}}}{V_i^{\text{g,ref}}} \right)^{-A} \ln \left(\frac{V_i^{\text{gain}}}{V_i^{\text{g,ref}}} \right) \right|. \tag{13}$$

It should be noted that σ_{G_i} goes towards zero when measurements are made at the reference gain voltage (e.g., for the channel sensitivity calibration described in the previous section). The gain calibration should be repeated with various ND filters to ensure linear operation over the entire range of signal intensities relevant for the experiment [24] and that gain voltages and anode currents remain within the specifications of the manufacturer. Sample PMT signals generated following this procedure are shown in Fig. 5, including an indication of the temporal range over which the PMT signal is averaged to obtain i_i^a and for which the variance is used to estimate $\sigma_{i_i^a}$. The increase in noise for higher signals is consistent with the standard Poisson–Gaussian noise model [59].

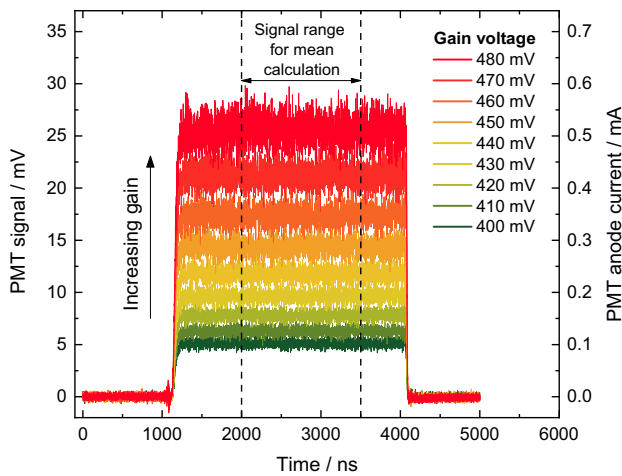


Fig. 5 Gated PMT signals for 50-Ω coupling and corresponding anode currents for a variation of gain voltages

2.3.4 Correction for variable optical components

For some LII experiments, additional optical components must be introduced to adapt to experimental conditions. For example, variable ND filters may be used to attenuate the light/signal intensity, or the collection optics may be adjusted to alter the collection solid angle. Usually, the calibration light source is placed at the LII probe volume position and the efficiency of collection optics is included in the PMT sensitivity calibration. In this study, we use an arrangement based around a collecting integrating sphere to separate the collection optics calibration from the PMT sensitivity calibration. The efficiency of the collection optics ϕ and the transmittance of ND filters τ are therefore incorporated as additional factors in the signal processing.

2.3.5 Summary of LII signal calibration

By combining the various calibration procedures in the preceding sections, the calibrated relative irradiance $J_{\lambda,i}^{\text{exp}}$ can be calculated from the measured signal response V_i^{meas} of the i th channel at time t by

$$J_i^{\text{exp}}(t) = \frac{\bar{D}_i G_i}{\tau_{ij} \phi_i} [V_i^{\text{meas}}(t) - V_i^{\text{baseline}}]. \tag{14}$$

This will act as the input to subsequent signal processing.

2.4 Spectroscopic model

Following calibration, LII signal processing proceeds with two consecutive steps: (1) calculation of a temperature trace from calibrated LII signals using a spectroscopic model and (2) inferring the quantities of interest (e.g., particle size)

by comparing the measured temperature traces to those obtained using a heat transfer model. The spectroscopic model is given by

$$J_i^{\text{mod}}(T_p) \propto f_V B_i \int_0^\infty p(d_p) C_{\lambda_i, \text{abs}}(d_p) I_{\lambda_i, \text{BB}}[T_p(d_p)] dd_p, \tag{15}$$

where $I_{\lambda_i, \text{BB}}$ and $C_{\lambda_i, \text{abs}}$ are the blackbody spectral intensity and wavelength-dependent absorption cross-section of a particular particle diameter at the center wavelength of the i th channel, respectively, which are integrated over the particle size distribution $p(d_p)$, and scaled by the volume fraction of particles in the measurement volume during the given laser pulse, f_V , and the geometry and optical efficiencies of the detection system B_i . For spherical nanoparticles, the spectral absorption cross-section $C_{\lambda, \text{abs}}$ is often calculated assuming the Rayleigh limit of Mie theory [60],

$$C_{\lambda, \text{abs}}(d_p) = \frac{\pi^2 d_p^3}{\lambda} E(m_\lambda), \tag{16}$$

provided that $\pi d_p / \lambda \ll 1$ and $|m_\lambda| \pi d_p / \lambda < 1$, where $E(m_\lambda)$ is the absorption function and m_λ is the complex index of refraction. In the current work, a monodisperse particle size distribution is assumed and the temperature is considered as an “effective” temperature of an ensemble of nanoparticles of the same size that is a biased estimate of the true mean particle temperature. Accordingly, Eq. (15) can be written as

$$J_i^{\text{mod}}(T_{p, \text{eff}}) \propto f_V B_i C_{\lambda_i, \text{abs}} \frac{2hc_0^2}{\lambda_i^5} \left[\exp\left(\frac{hc_0}{k_B \lambda_i T_{p, \text{eff}}}\right) - 1 \right]^{-1}. \tag{17}$$

The wavelength-independent properties of Eqs. (16) and (17) (i.e., the particle diameter, the particle volume fraction, and the detection efficiency) can be combined into a summary parameter [61], Λ , which further simplifies Eqs. (16) and (17) to

$$J_i^{\text{mod}}(T_{p, \text{eff}}, \Lambda) \propto \Lambda \frac{E(m_{\lambda_i})}{\lambda_i} I_{\lambda_i, \text{BB}}[T_p(d_p)] = \Lambda \frac{E(m_{\lambda_i})}{\lambda_i} \frac{2hc_0^2}{\lambda_i^5} \left[\exp\left(\frac{hc_0}{k_B \lambda_i T_{p, \text{eff}}}\right) - 1 \right]^{-1}. \tag{18}$$

For the calculation of temperature traces from measured irradiances, two methods are widely used: (1) two-color pyrometry and (2) fitting of the spectral incandescence to two or more spectral measurements bands or to full spectra. The temperature calculation is repeated at each measurement time to obtain a temporally resolved temperature trace that serves as an input to the heat transfer model used in

determining the nanoparticle size and other attributes of the aerosol.

Two-color pyrometry (e.g., [7, 14, 18, 19]) requires calibrated LII signals at two independent wavelengths and involves taking the ratio of the spectral irradiance at both wavelengths

$$T_{p,\text{eff}} = \frac{hc_0}{k_B} \left(\frac{1}{\lambda_2} - \frac{1}{\lambda_1} \right) \left[\ln \left(\frac{J_1^{\text{exp}}(t) E(m_{\lambda_2})}{J_2^{\text{exp}}(t) E(m_{\lambda_1})} \left(\frac{\lambda_1}{\lambda_2} \right)^6 \right) \right]^{-1}, \tag{19}$$

where $T_{p,\text{eff}}$ is the effective particle temperature, h is the Planck constant, c_0 is the speed of light in vacuum, k_B is the Boltzmann constant, and λ_i is the center wavelength of the detector bandpass filter. This is the default method used by practitioners.

When two or more spectral detection channels are available, the temperature can be inferred through nonlinear least-squares regression to the experimentally determined calibrated irradiances, J_i^{exp} :

$$T_{p,\text{eff}} = \arg \min_{T_p, \Lambda} \left\{ \sum_i \left[\frac{J_i^{\text{exp}}(t) - J_i^{\text{mod}}(T_p, \Lambda)}{\sigma_i} \right]^2 \right\}. \tag{20}$$

For multi-wavelength pyrometry using more than two channels, the variance of different channels needs to be considered as standard deviation of the measurement data σ_i . The magnitude of the variance of each channel is related to detector noise, detector sensitivity, and the measured signal intensity and can vary significantly between channels. It can be experimentally determined by pooling the results of multiple laser shots or estimated using a noise model as outlined in Ref. [59]. Assigning equal influence of all channels by assuming $\sigma_i = 1$ would falsely give more influence to a channel that is affected by higher uncertainty and thus bias the inferred temperatures.

2.5 Statistical considerations

There is an increasing trend in the LII community to account for how measurement noise and model-parameter uncertainty affect quantities derived from LII measurements [10–12, 62, 63]. In this study, the Bayesian approach was used to investigate the influence of calibration parameters and measurement noise on pyrometrically determined temperatures from multi-color LII detection using photomultiplier tubes. The Bayesian approach treats the various quantities as random variables that follow some distribution [64]. The observations contained in \mathbf{b} and the quantities of interest (QoI, here the effective temperature) are then related by way of a likelihood, $p_{\text{like}}(\mathbf{b}|T_{p,\text{eff}})$, which defines the likelihood of the observed data (spectral incandescence, or, more

fundamentally, PMT voltages) occurring for a hypothetical temperature. Assuming that the noise and model errors in \mathbf{b} are independent and normally distributed, the likelihood can be phrased as a multivariate normal distribution

$$p_{\text{like}}(\mathbf{b}|T_{p,\text{eff}}) = \frac{1}{\prod_i (2\pi)^{1/2} \sigma_{b,i}} \exp \left(-\frac{1}{2} \sum_i \left[\frac{b_i(t) - b_i^{\text{mod}}(T_{p,\text{eff}}, \Lambda)}{\sigma_{b,i}} \right]^2 \right), \tag{21}$$

where b_i^{mod} is a model of the measured quantity and $\sigma_{b,i}$ is the standard deviation of the measurement data for the i th channel. Moreover, the maximum of this distribution corresponds to the weighted least-squares solution, that is

$$T_{p,\text{eff}} = \arg \max_{T_{p,\text{eff}}, \Lambda} [p_{\text{like}}(\mathbf{b}|T_{p,\text{eff}})] = \arg \min_{T_{p,\text{eff}}, \Lambda} \sum_i \left[\frac{b_i(t) - b_i^{\text{mod}}(T_{p,\text{eff}}, \Lambda)}{\sigma_{b,i}} \right]^2. \tag{22}$$

In the current study, the data are taken as the average signal measured by the PMTs, corrected for the baseline, the transmittance of the ND filters, and the efficiency of the collection optics, which are considered deterministic parameters,

$$b_i(t) = \frac{1}{\tau_{ij} \phi_i} (\bar{V}_i^{\text{meas}}(t) - V_i^{\text{baseline}}), \tag{23}$$

where the overbar indicates an average over multiple shots and i denotes the i th channel. This quantity is normally distributed according to the central limit theorem, justifying the form chosen for the likelihood. Moreover, in this case, $\sigma_{b,i}$ is the standard deviation of the mean signal, corresponding to the standard deviation over multiple shots reduced by the square root of the number of shots and by τ_{ij} and ϕ_i . By this definition, b_i^{mod} is the modeled data evaluated at some hypothetical $T_{p,\text{eff}}$, which incorporates the gain correction function G_i and the relative PMT sensitivity calibration factor D_i . In this study, we focus on the PMT sensitivity calibration and consider only measurements at the gain reference voltage, so that $G_i = 1$. The expected signal for the i th channel is then

$$b_i^{\text{mod}}(T_{p,\text{eff}}, \Lambda) = \frac{1}{D_i G_i} \Lambda \frac{E(m_{\lambda_i})}{\lambda_i} \frac{2hc_0^2}{\lambda_i^5} \left[\exp \left(\frac{hc_0}{k_B \lambda_i T_{p,\text{eff}}} \right) - 1 \right]^{-1}. \tag{24}$$

Unfortunately, this approach neglects the uncertainty introduced through the calibration procedure described above. This can be incorporated by defining the calibration factors as additional nuisance parameters to be solved along with the unknown pyrometric temperature,

$\theta = [D_1, D_2, \dots, D_n]^T$. These can be incorporated into the likelihood by adding them to the vector of QoIs, such that

$$p_{\text{like}}(\mathbf{b}|T_{p,\text{eff}}, \theta) = \frac{1}{\prod_i (2\pi)^{1/2} \sigma_{b,i}} \exp\left(-\frac{1}{2} \sum_i \left[\frac{b_i(t) - b_i^{\text{mod}}(T_{p,\text{eff}}, \Lambda, \theta)}{\sigma_{b,i}}\right]^2\right), \tag{25}$$

where b_i^{mod} becomes a function of both $T_{p,\text{eff}}$ and θ . In considering the nuisance parameters, it is crucial to incorporate prior information known about the nuisance parameters and QoI before a measurement, via the prior probability, $p_{\text{pri}}(\theta)$, in addition to information extracted from the data [64]. The result is the posterior probability, $p(T_{p,\text{eff}}, \theta|\mathbf{b})$, which is described by Bayes' equation. If the nuisance parameters and QoI are statistically independent before the measurement [63] and no prior information is known about $T_{p,\text{eff}}$ a priori, the posterior is given by

$$p(T_{p,\text{eff}}, \theta|\mathbf{b}) = \frac{p_{\text{like}}(\mathbf{b}|T_{p,\text{eff}}, \theta)p_{\text{pri}}(\theta)}{p(\mathbf{b})}, \tag{26}$$

where $p(\mathbf{b})$ is the evidence that acts to scale the product of the priors and likelihood so that the law of total probability is satisfied. Information known about the nuisance parameters are also encoded in a normal distribution,

$$p_{\text{pri}}(\theta) \propto \exp\left\{-\frac{1}{2} \sum_i \left[\frac{\theta_i - \mu_{\theta,i}}{\sigma_{\theta,i}}\right]^2\right\}. \tag{27}$$

where $\mu_{\theta,i}$ and $\sigma_{\theta,i}$ are the expected value and standard deviation of each calibration coefficient. The distribution of the effective temperature alone can then be derived by marginalizing over the nuisance parameters

$$p(T_{p,\text{eff}}|\mathbf{b}) = \frac{1}{p(\mathbf{b})} \int p_{\text{like}}(\mathbf{b}|T_{p,\text{eff}}, \theta)p_{\text{pri}}(\theta)d\theta. \tag{28}$$

Moreover, the maximum of the posterior distribution, called the maximum a posteriori (MAP) estimate,

$$\begin{aligned} [T_{p,\text{eff}}, \theta]^{\text{MAP}} &= \arg \max_{T_{p,\text{eff}}, \Lambda, \theta} [p(T_{p,\text{eff}}, \theta|\mathbf{b})] \\ &= \arg \min_{T_{p,\text{eff}}, \Lambda, \theta} \left\{ \sum_i \left[\frac{b_i(t) - b_i^{\text{mod}}(T_{p,\text{eff}}, \Lambda, \theta)}{\sigma_{b,i}}\right]^2 + \sum_i \left[\frac{\theta_i - \mu_{\theta,i}}{\sigma_{\theta,i}}\right]^2 \right\} \end{aligned} \tag{29}$$

represents the most probable value of $T_{p,\text{eff}}$ and θ based on the observed data and priors. The posterior distribution also indicates the uncertainty attached to each inferred temperature. This information can then be compared across different channel combinations to evaluate the combined uncertainty introduced by the calibration coefficients and measurement noise.

3 Experiment

Consider now a multi-color LII detection setup combined with various calibration light sources.

3.1 Calibration light sources

For this study, four different light sources are used: (1) halogen lamps built into an integrating sphere (IS), (2) a laser-driven light source (LDLS), (3) a stabilized tungsten halogen light source (SLS), and (4) light-emitting diodes (LED). The IS and the LDLS have been calibrated previously for spectral irradiance by external certified calibration laboratories. The key parameters for all light sources are summarized in Table 1. The center wavelengths of the LEDs closely match the detector's bandpass center wavelengths and were used in a previous study to investigate the linearity of PMTs [24]. The characterization procedure of the light sources is described in Sect. 4.1.2.

3.2 Detector arrangement

Figure 6 gives a schematic overview of the experimental setup. The central element is an integrating sphere (diameter 5 cm, Thorlabs IS200-4) with four ports that ensures reproducible radiance measurements for any attached light source and detector. The broadband light sources and the LED array (3 LEDs) are connected to two ports and the spectral emission profiles can be observed with a fiber-coupled spectrometer (Ocean Optics USB-4000). As an alternative, an optical fiber (core diameter: 1000 μm) is used for coupling to an LII experiment where the light is collected via fiber-coupled collection optics. The collection optics consists of two achromatic doublets with 100 mm and 150 mm focal lengths. Homogenized light from the integrating sphere exits through a pinhole and is collimated before passing an ND-filter wheel (100, 79, 50, or 10% transmission) and two dichroic beam splitters with edge wavelengths of 605 nm (FF605-Di02) and 740 nm (FF740-Di01) or a 50:50 beam splitter (Thorlabs BSW10R). The light is then focused on to four gated PMTs: three with a multi-alkali (MA) photocathode (Hamamatsu H11526-20) and one with a super bi-alkali (SBA) photocathode (Hamamatsu H11526-110).

Table 1 Light sources used for the calibration procedure in this paper

	IS	LDLS	SLS	LED
Type	Halogen lamps built into an integrating sphere	Laser-driven light source	Stabilized tungsten halogen light source	Light-emitting diodes
Model	K-150WH (LOT-Oriel)	EQ-99X LDLS (Energetiq)	SLS201L (Thorlabs)	EOLD-505-534 EOLD-685-524 EOLD-810-525 (EPIGAP)
Power supply	SLP120-80 (Gossen-Metrawatt)	Internal	Internal	GPS-2303 (GW Instek)
Calibration	Dec. 2016 opto.cal (Switzerland)	Sept. 2017 PTB (Germany)	–	–
Spectrum	Broadband	Broadband	Broadband	Narrow band around center wavelength
Spatial intensity profile	Homogeneous	Spatial intensity profile not homogeneous, coupling with diffuser optics/integrating sphere recommended		
Advantages	Homogeneous spatial intensity profile, reduces alignment errors	Strong emission from UV to near-infrared enables covering most detection wavelength bands	Compact and low cost	Intensity can be individually controlled for each LED; very low cost
Disadvantages	Weak emission in the UV increases uncertainty of calibration at short detection wavelengths	Xenon plasma atomic emission lines can interfere with detection wavelength bands and introduce errors (very strong > 820 nm)	Weak emission in the UV increases uncertainty of calibration at short detection wavelengths	Center wavelengths should match detection wavelengths, but not all center wavelengths are commercially available
Price	Moderate	High	Low	Very low

For spectral separation, bandpass filters are attached to the PMTs that are specified for spectral ranges often used for two-color LII measurements [65] with center wavelengths and bandwidths (FWHM) of 500 ± 13 nm (PMT1 and PMT2, Semrock FF01-500/24), 684 ± 13 nm (PMT3, Semrock FF02-684/24), and 797 ± 9 nm (PMT4, Semrock FF01-800/12). For the LII measurements, soot particles are heated by a pulsed (10 ns FWHM) Nd:YAG laser at 1064 nm (Continuum, Powerlite 7000). A circular 3.2-mm aperture is used to shape the laser profile. Signals are collected with a 500-MHz oscilloscope (PicoScope 6404C) with an ADC resolution of 8 bit and 0.8-ns sampling intervals.

The use of an integrating sphere within the LII detection optics makes the system more robust to alignment errors and thus variations in the intensity of the attached light sources. Furthermore, it allows superimposing the light from various sources for linearity measurements and facilitates comparison of detection devices without introducing additional optical elements that could bias the spatial intensity distribution. However, the integrating sphere could introduce a distortion in the temporal intensity measurement that needs to be considered [61, 66]. Multiple reflections within the sphere result in a long light path compared to the nanosecond time resolution of the detector, which temporally stretches the signal. This effect

can be identified as temporal blurring and the FWHM was determined for this sphere as below 12 ns.

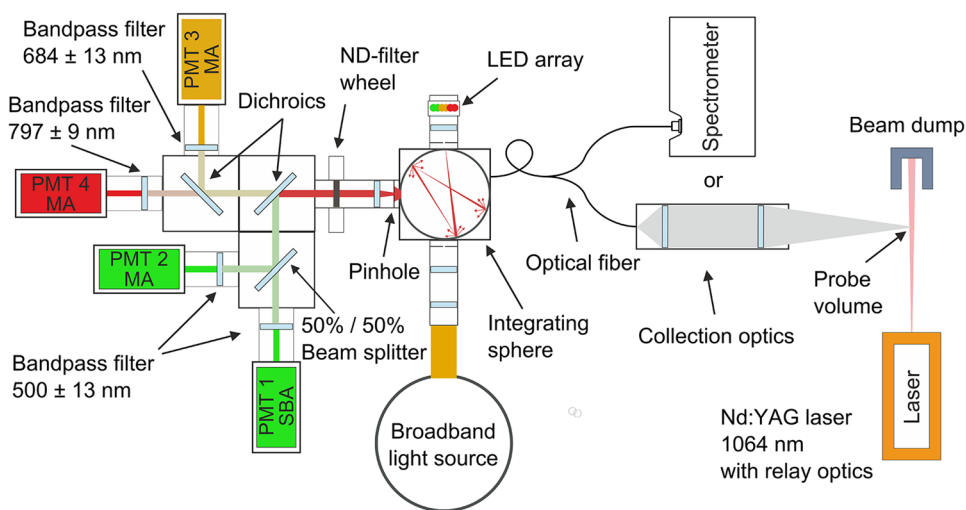
3.3 Laminar diffusion flame

Validation measurements are performed using a laminar non-premixed flame [67] that has been the subject of numerous TiRe-LII studies [1]. The burner is operated at its standard conditions of 0.194 standard liters per minute (slm) ethene (C_2H_4) and 284 slm air, and measurements are performed at the standard reference position of 42 mm height above burner (HAB). For this position, the gas temperature was previously determined to be 1730 ± 25 K [67] and 1740 K [68], respectively, using coherent anti-Stokes Raman spectroscopy (CARS).

4 Methodology and results

The calibration procedure outlined above, including consideration of uncertainties, is demonstrated with the presented detector arrangement and light sources. The acquired set of calibration factors is used to calibrate LII signal traces obtained from in-flame measurements and the uncertainty of the calibration factors is propagated through the analysis to

Fig. 6 Four-PMT setup with collecting integrating sphere, LED array, broadband light source, and a fiber-coupled spectrometer



evaluate the corresponding uncertainty in the inferred temperatures for different channel combinations.

4.1 Calibration

The calibration procedure can be divided into five steps: (1) spectrometer validation, to ensure linearity and a correct wavelength calibration; (2) calibration of the transmission through ND filters; (3) measurement of the spectral transmission through collection optics and sensitivity to chromatic aberration; (4) light-source characterization for spectral irradiance; and (5) PMT gain and sensitivity calibration. All of the light sources are operated for at least 60 min before the experiment to ensure thermal equilibration. The intensity of each LED is adjusted with series resistors to ensure approximately equal intensity levels for all channels.

4.1.1 Characterization of collection optics

A configuration of the collection optics with achromatic doublets is compared to the configuration with uncoated plano-convex lenses to investigate the influence of chromatic aberration. For the alignment/focusing of the collection optics, a fiber-coupled diode laser (635 nm) is used. The influence of chromatic aberration is investigated relative to this wavelength.

The spectrometer is attached to the fiber port of the integrating sphere broadband light source (IS) (Fig. 7—Position A) and the calibrated spectrum of the light source is recorded as a reference. The spectrometer is then attached to Position B to measure the transmitted light through the collection optics. Dividing the reference spectrum by the attenuated spectrum gives then the spectrally resolved transmittance of the collection optics. To experimentally identify the influence of chromatic aberration, a variable aperture (VA) is mounted in front of the IS light source and a fiber-coupled diode alignment laser is attached to Position B. The opening

diameter of the VA is then reduced to match the fiber core diameter (1000 μm) as visualized by the diode laser.

Figure 8 shows the measured spectra at Position A (blue) and Position B with the variable aperture opened 1 mm (yellow) and opened 4 mm (red) for achromatic doublets (a) and uncoated plano-convex lenses (b). While the spectra measured with the achromatic lenses show almost no differences between the aperture opening diameters, the normal lenses reveal significant influence of chromatic aberration with decreasing opening diameters. As a consequence, for wavelengths longer and shorter than the alignment wavelength, the focal length shifts and less light are collected by the fiber. Similar effects are expected when focusing light on to the entrance slit of a spectrometer or a pinhole for spatial filtering. For the achromatic lenses, the reduced intensity, measured for wavelengths longer than 700 nm can be explained by the reduced spectral transmittance of the lenses as specified by the manufacturer.

For LII measurements, it is often desired to spatially limit the detection volume by imaging the signal light through a pinhole, a slit, or by focusing the signal light on the entrance face of a fiber (which then acts as a pinhole). The resulting detection solid angle, combined with the spatial laser profile, defines the probe volume. When these components are used without achromatic optics, chromatic aberration can strongly bias pyrometrically determined temperatures. The comparison of two-color peak temperatures at detection wavelengths of 500 and 800 nm for the conditions described in Sect. 4.2 revealed a reduction in the peak temperature of 500 K for the lenses affected by chromatic aberration relative to the achromatic doublets. In several recent LII studies, achromatic lenses are already standard components of the collection optics [20, 69, 70]. To account for the transmission through collection optics, a correction for the collection efficiency, ϕ_i , for each channel is included in the signal processing. The values for ϕ_i for the achromatic lenses used in this study are

1.0, 0.98, and 0.87 for the 500-, 684-, and 797-nm channel, respectively; they are included in Eqs. (14) and (23).

4.1.2 Characterization of the calibration light sources

The arrangement shown in Fig. 6 can be used to characterize various light sources and calibrate the PMT setup. For these measurements, the spectral reflectivity of the collecting integrating sphere (IS200-4) is assumed to be flat ($99 \pm 0.2\%$) between 350 and 850 nm as specified by the manufacturer. For the analysis, the fiber-coupled spectrometer is attached to the fiber port to collect spectra for the various light sources [i.e., halogen lamps built into an integrating sphere (IS), laser-driven light source (LDLS), stabilized tungsten halogen lamp (SLS), and the three continuously operated LEDs].

The spectra collected with the spectrometer (Fig. 9) must be corrected for the dark signal. The spectra of the light sources with known calibration (IS and LDLS) are then used to calculate two independent instrument sensitivity spectra (Fig. 10) that can then be used to calibrate other light sources.

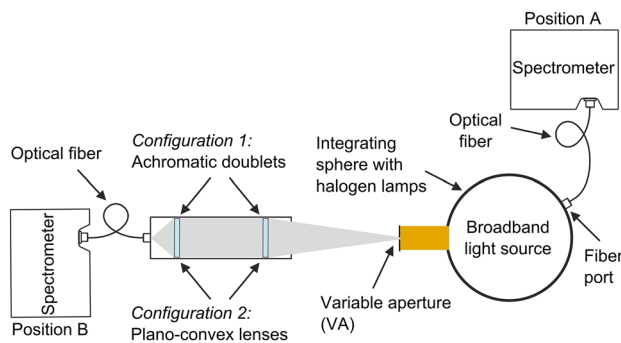


Fig. 7 Setup for spectrometer calibration and characterization of the collection optics

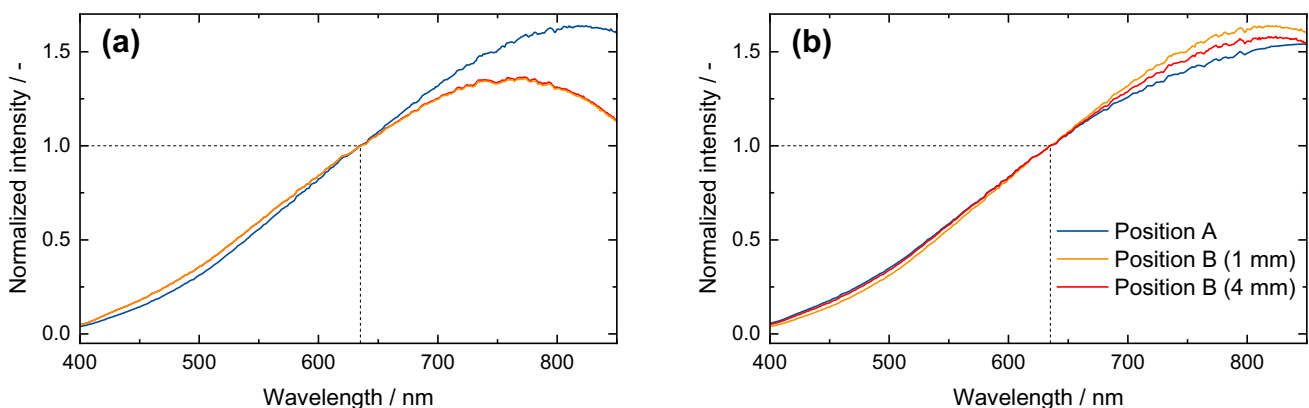


Fig. 8 Measured spectra of the reference light source at Position A (blue) and Position B with the variable aperture 1 mm opened (yellow) and 4 mm opened (red) for **a** achromatic doublets and **b** uncoated plano-convex lenses

The spectrometer sensitivity peaks at 518 nm. The instrument sensitivity spectrum becomes noisier at shorter wavelengths due to the low intensity of the IS below 450 nm and the low sensitivity of the spectrometer at these wavelengths. The higher emission of the LDLS results in a smoother instrument sensitivity spectrum, particularly at lower wavelengths. Unfortunately, the fluctuating intensity of atomic emission lines from the xenon plasma results in narrow wavelength-specific anomalies that lead to errors in the LDLS calibration spectrum.

Figure 11 shows the relative intensities of all light sources, calculated from the calibration spectra of the IS (a) or the LDLS (b). The intensity of the IS decreases continuously towards the UV and can thus introduce errors in the calibration of shorter wavelengths. The LDLS intensity spectrum is stronger in the near-UV and is therefore suitable for calibration at short detection wavelengths (< 450 nm); however, for wavelengths longer than 820 nm, measurements can be biased by strong atomic emissions from the plasma source. The error between the two calibration sources is smaller than 1% for the detection wavelengths used in this study. Therefore, the IS calibration spectrum is used to calibrate the spectrometer sensitivity in subsequent sections.

The light exiting the pinhole from the collecting integrating sphere is now characterized and can be used for the relative sensitivity calibration of the PMTs. The characterization of the LEDs revealed that the LED peak wavelengths differed slightly from the manufacturer specification and were determined as 500, 689, and 820 nm.

4.1.3 PMT calibration

The arrangement shown in Fig. 6 is used to calibrate the PMTs. The gain correction and sensitivity calibration are related to the same reference voltage (i.e., 450 mV). Two hundred signals are collected at 10 Hz with a PMT gate time

of 8 μs (same as for the LII measurements). The widths of the temporal sections were arbitrarily chosen as 400 ns (A) and 3000 ns (B) according to Fig. 3.

4.1.3.1 PMT gain calibration Any stable light source can be used for calibrating the PMT gain. The measurements in this section are performed using the LDLS as its spectral intensity is nearly uniform over the detection spectrum. The gain calibration is performed at gain control voltages between 300 and 550 mV. The maximum gain voltage for each channel is set so as to ensure that the measured signal does not exceed the ADC voltage range of the oscilloscope. The gain characteristics are investigated by varying the gain voltage from the maximum possible value down to 300 mV in -2 mV increments. The signal response for each voltage is measured after 5 s of stabilization. This sequence is then repeated with 1 mV offset and -2 mV increments to achieve a total resolution of 1 mV. If the light source exhibits a temporal drift, an offset in the data from the two

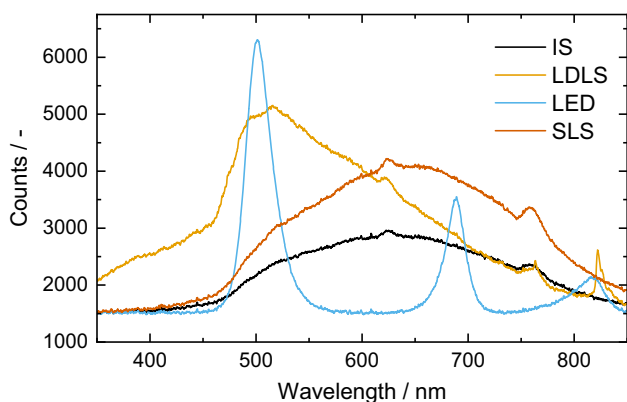
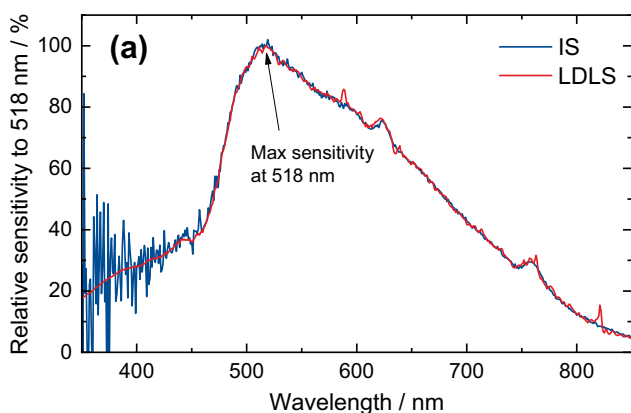


Fig. 9 Measured uncorrected light source emission intensities convolved with the instrument function of the fiber-coupled spectrometer



sequences can be identified. To increase reproducibility, a LABVIEW algorithm is used to automate the calibration sequence. Figure 12 shows the ND-filter-corrected results for PMT 1 and 2 across three ND filters (i.e., 10, 50, and 79% transmission). For PMT 1 (Fig. 12a), the offset between the filter curves can be interpreted as nonlinearity over the varying light levels.

For PMT 2, the gain correction function is determined for three ND filters and is shown in Fig. 13. This analysis gives the gain correction function G_i and its standard deviation σ_{G_i} , as described in Sect. 2.3.3. The scatter in the signal data for gain voltages below 400 mV indicates an unstable behavior of the PMTs such that these gain voltages are avoided.

4.1.3.2 Relative PMT sensitivity calibration The light sources described in Sect. 3.1 are used for the relative PMT sensitivity calibration. The PMT response is recorded for various ND-filter transmissions and for a constant gain control voltage (i.e., 450 mV) (Fig. 14). Calibration factors for all channels and light sources can then be calculated according Sect. 2.3.2, and the standard deviation from the complete set can be used in an uncertainty analysis of the calibration.

The calculated calibration factors are summarized in Fig. 15. PMT 1 shows strong non-linear behavior with increasing light level, which causes the calibration factor to increase with increasing light level, while PMT 2, which measures at the same wavelength, is not affected. This can be traced back to the photocathode material of PMT 1, which is more sensitive to nonlinearities [24]. The non-linear behavior can also be observed for PMT 3 and PMT 4, albeit to a lesser extent.

For the calibration of PMT 4, an offset between the signal detected with the LEDs and the other light sources is visible. This is attributed to the fact that the detection center wavelength of PMT 4 (i.e., 797 ± 9 nm) is offset from the LED center wavelength (820 nm) by more than the bandpass filter

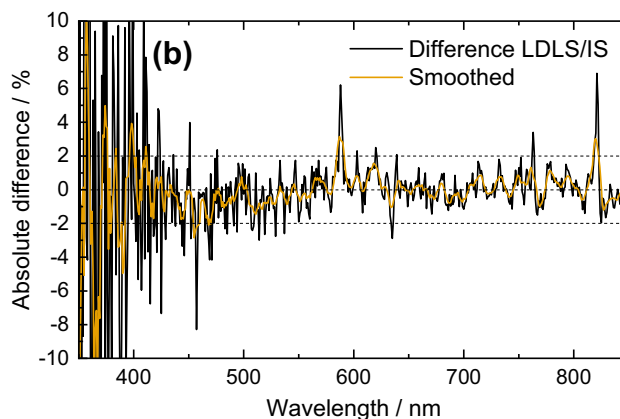


Fig. 10 a Instrument sensitivity calculated from the calibration spectrum of the halogen lamp/integrating sphere light source (IS) and the laser-driven light source (LDLS). b Absolute deviation between the two calibrations methods

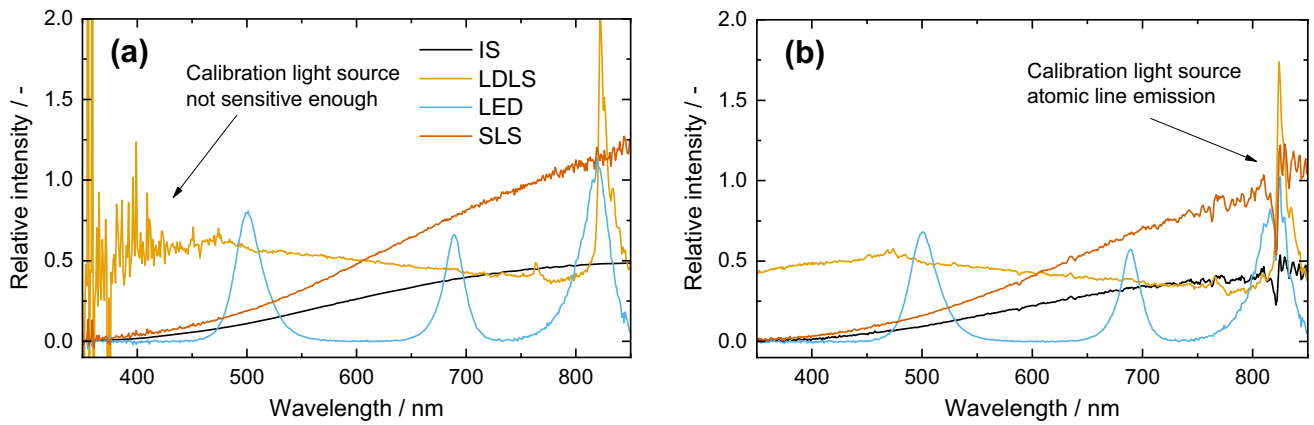


Fig. 11 Calibrated light source intensity spectra, calculated from **a** the IS calibration and **b** the LDLS calibration

FWHM. The integral calculation method (cf. Eq. 3) is more sensitive to intensity fluctuations and wavelength errors when the edge of the narrowband spectrum is analyzed over the center region. The mean calibration factors used for the further analysis are summarized in Table 2.

4.2 Reference LII experiment

The uncertainty in the calibration is incorporated into the signal processing of the measured data from an LII experiment to determine the uncertainty in the temperature trace. For the present analysis, we assume $E(m_i)$ to be wavelength independent [62]. Measurements are carried out at the gain reference voltage of all PMTs (i.e., 450 mV) to neglect the error introduced by the gain correction function. The laser energy is adjusted to obtain a fluence of 1 mJ/mm², and LII signals for 100 laser shots are acquired. Figure 16 shows the

baseline-corrected LII signal traces for all four channels. Four data points are selected for further analysis: (A) flame emission without laser interaction, (B) the LII signal peak, and the LII signal at (C) 1 μs, and (D) 2.5 μs after the peak.

Spectral fitting is investigated using various channel combinations, taking into account uncertainties from the detector calibration and measurement noise. Table 3 shows the channel combinations used for the spectral fitting. T1 represents the spectral fitting of all channels, and T2–T6 represent all possible two-color combinations given the four available channels, excluding the combination of channels 1 and 2, which are at the same wavelength.

The standard deviations of the various calibration factors, calculated as shown in Table 2, are used as a prior for the uncertainty analysis and the standard deviation from the multi-shot averaging is incorporated in the calculation of the likelihood (cf. Sect. 2.5). The credibility intervals in

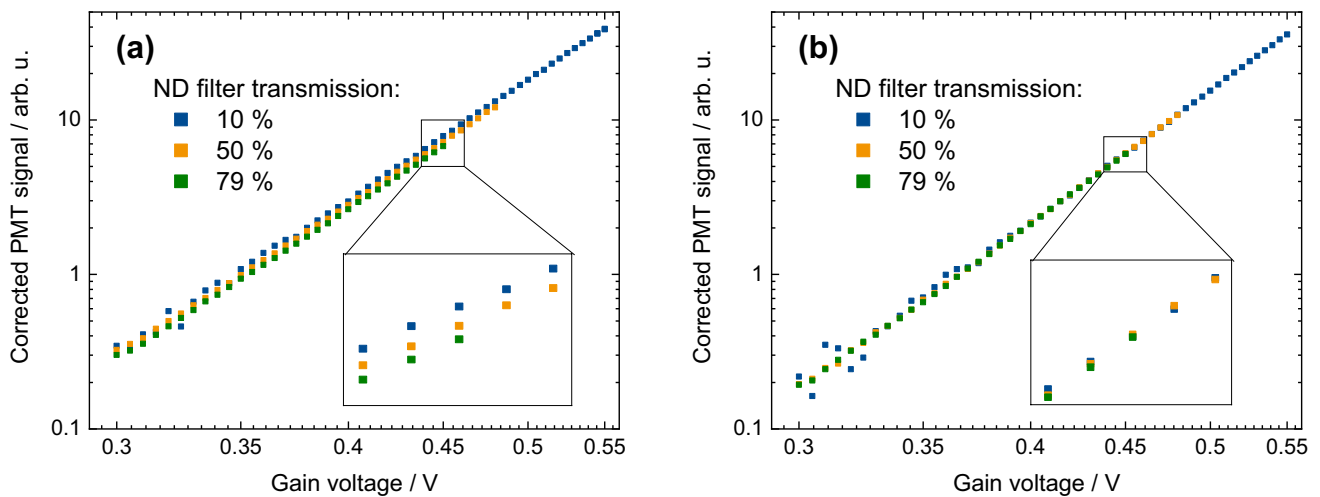


Fig. 12 Mean signal as a function of gain voltage for **a** PMT 1 and **b** PMT 2 corrected for the respective ND-filter transmission

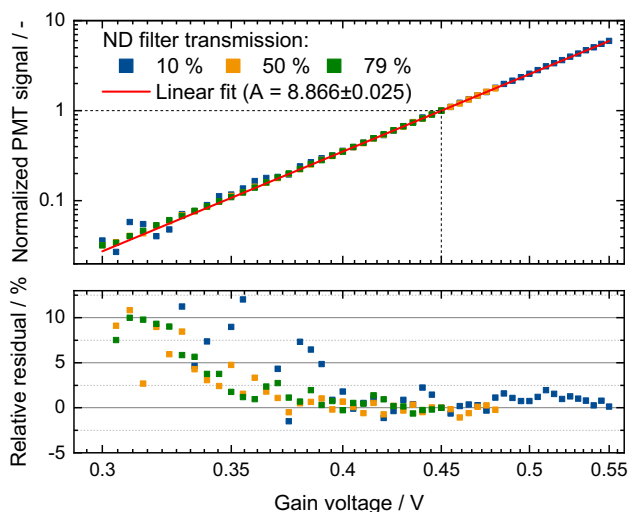


Fig. 13 Gain-correction function with best fitting coefficient $A = 8.866 \pm 0.025$ for PMT 2 and the residual between the experimentally determined gain correction function and the measurements. The dashed line indicates the gain reference voltage used for the normalization

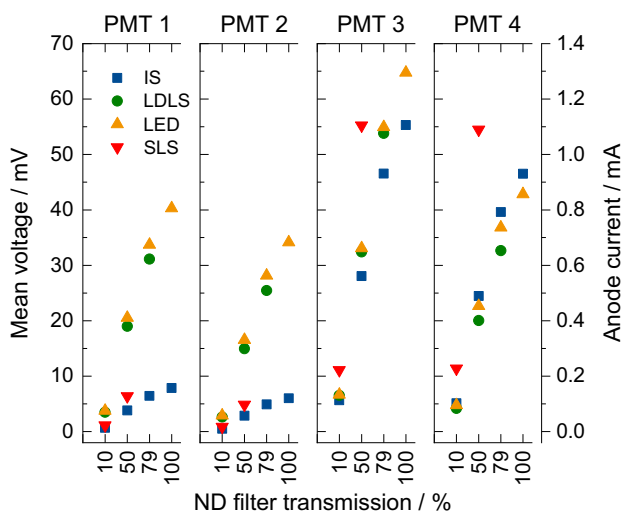


Fig. 14 Measured anode currents and corresponding signal voltages for 50-Ω coupling for various ND-filter transmissions for IS, LDLS, SLS, and LEDs

this section represent the interval in which the measurement values lie with a probability of 95%.

Figure 17 shows the spectral fits for all channel combinations for the temporal sections A–D. The difference in temperature between the different channel combinations cannot be explained by the uncertainty introduced by measurement noise and the calibration. This could indicate that the soot absorption function has some variation with respect to wavelength or that there may be additional chromatic aberrations

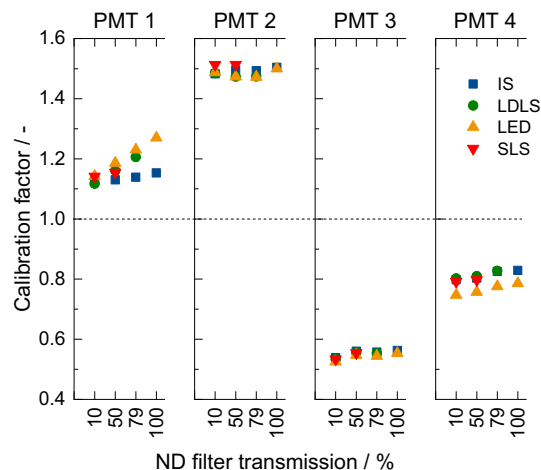


Fig. 15 Comparison of sensitivity calibration factors from different light sources for various ND-filter transmissions

Table 2 Mean calibration factors with standard deviation

	Channel 1 (500 nm)	Channel 2 (500 nm)	Channel 3 (684 nm)	Channel 4 (797 nm)
\bar{D}_i	1.166	1.490	0.548	0.796
σ_D	0.045	0.015	0.012	0.025

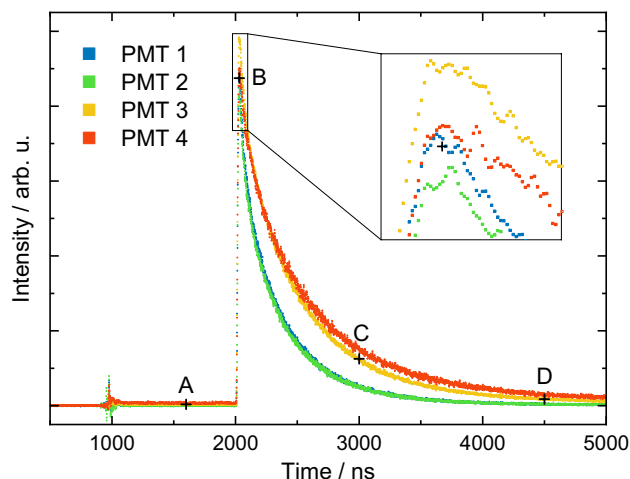


Fig. 16 LII signal traces for 1 mJ/mm^2 ; letters A–D indicate points in time used for further analysis

within the LII setup that were not included in the calibration procedure. The signals of channel 1 and 2 are measured at the same bandpass filter wavelengths and therefore they should match after calibration. However, for a strong signal (e.g., the peak intensity), the signal from channel 1 is higher than channel 2. This is because the calibration of

Table 3 LII signal channels used for the calculation of the particle temperature traces

	Channel 1 (500 nm)	Channel 2 (500 nm)	Channel 3 (684 nm)	Channel 4 (797 nm)
T1	x	x	x	x
T2	x		x	
T3	x			x
T4		x	x	
T5		x		x
T6			x	x

PMT 1 is strongly affected by nonlinearities, which leads to an overestimation of the signals in the experiment. This could lead to differences in the evaluated temperatures of

100–200 K. Weak signals (i.e., A and D) are affected by a low signal-to-noise ratio and, while containing large discrepancies between the channel combinations, are associated with large uncertainties (up to ± 442 K).

It can be seen that the temperatures determined by two-color ratios, Eq. (17), (T2–T6) are very sensitive to calibration errors. In principle, these estimates can be made more robust by increasing the number of detection wavelengths (T1). However, other sources of errors may be introduced into the analysis beyond that which is considered in this study. For example, the calibration light source spectrum could have changed due to lifetime drift (i.e., bulb coating, deposits on optical components). Polydispersity [71, 72] or non-uniform laser heating [69, 73] can cause the particles in the probe volume to be heated to different temperatures

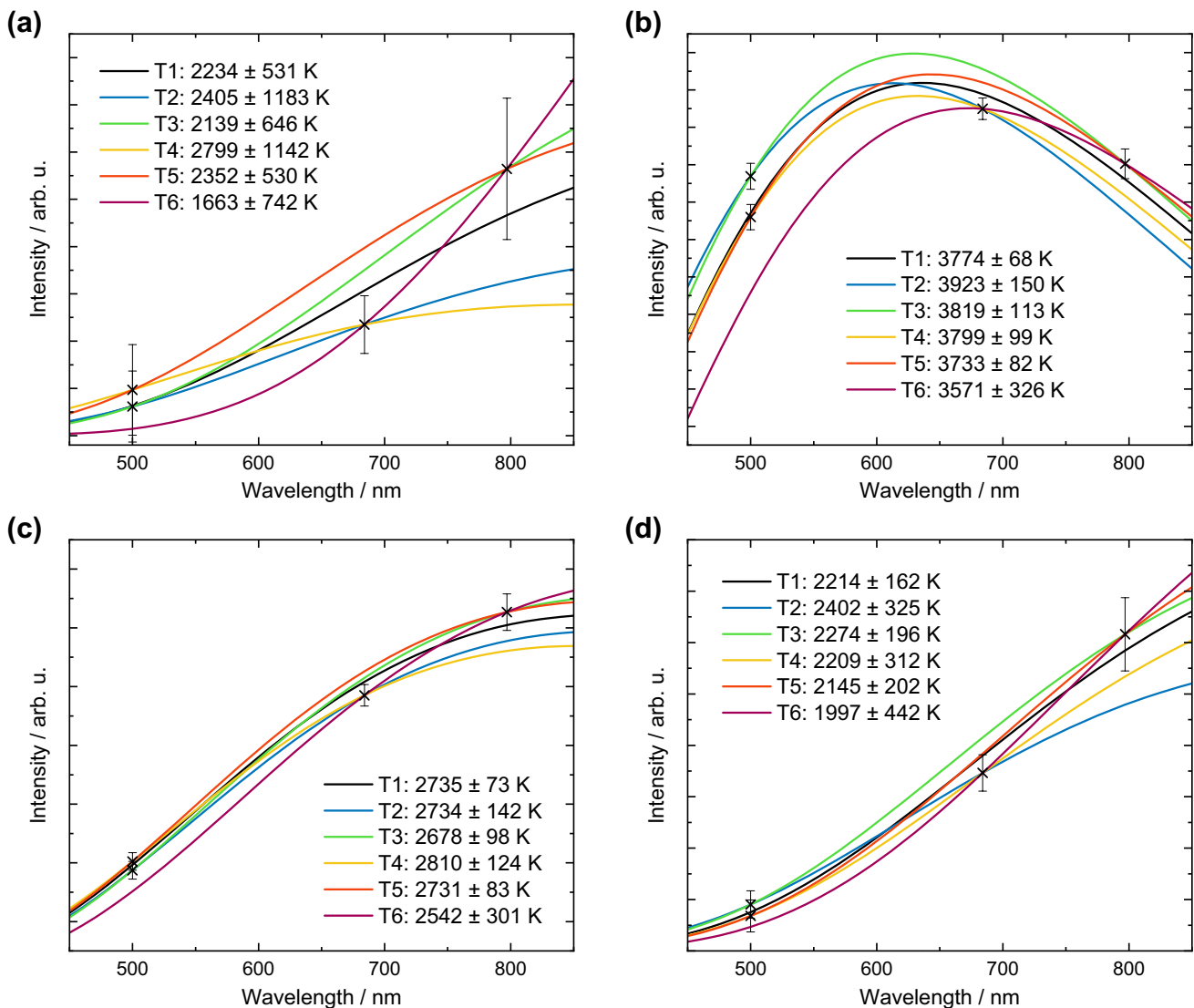


Fig. 17 Spectral fits of data as indicated in Fig. 16 for all temperature traces (T1–T6). Error bars indicate the standard deviation of the measurement for each data point σ_b . **a** Flame emission without laser interaction, **b** LII signal peak, and the LII signal at **c** 1 μ s and **d** 2.5 μ s after the peak

such that the measured incandescence spectrum is poorly represented by a single particle temperature. Further, the present study did not consider uncertainties in the radiative properties of the nanoparticles, which, especially in the case of soot, are highly uncertain and could vary significantly with wavelength.

5 Conclusions

This study demonstrates the detector calibration methodology for multi-color time-resolved LII measurements. The calibration procedure consists of: (1) baseline correction, (2) sensitivity calibration, (3) gain calibration, and (4) calibration of variable optical components. Multiple light sources are compared and calibration factors at various light levels are determined. A reference LII experiment is performed on a laminar diffusion flame to quantify the uncertainties introduced by the calibration. A Bayesian approach is used to propagate uncertainties in the calibration procedure and measurement to those in LII temperature traces.

When using a light source for calibration, the spectral profile should be compared with the detection wavelength band for lamp artifacts (i.e., atomic plasma emission). For LEDs, proper selection of the peak wavelengths and bandwidths according to the bandpass filter ranges is essential.

While PMTs are normally assumed to behave linearly, this assumption is often invalid in the initial phase of the signal trace where there are sharp features in LII signals. This work showed that nonlinear effects can impact the calibration, leading to biased calibration factors that result in a larger signal amplitude and thereby influence the pyrometrically determined temperature. Repeated measurements at different light levels using multiple ND filters can be used to diagnose nonlinear detector response.

Chromatic aberration of the detection optics can also introduce significant errors into the detector calibration and the measurement data used in the spectroscopic model. If the system is affected by chromatic aberration, this effect cannot be easily identified during calibration. In this work, a fiber-coupled measurement arrangement is presented that can identify chromatic errors in the collection optics. This effect can be avoided using achromatic lenses, though one must be aware that these lenses are often optimized over a limited wavelength range.

Apparent particle temperatures are determined by applying pyrometry to all possible two-color channel combinations and by fitting a spectrum to all four channels simultaneously. The temperatures determined from the various two-color ratios often differed by up to several hundred Kelvin, highlighting the weakness of two-color ratio pyrometry. This is affirmed by the fact that the largest uncertainties are encountered when combining two-color pyrometry with the

two longest detection wavelengths (i.e., 684 and 800 nm), while the lowest uncertainties are encountered when fitting a spectrum to all of the detection channels simultaneously. This suggests that one should always use spectral fitting to multiple wavelengths, whenever possible. However, additional aspects that can affect the analysis need to be considered to affirm this conclusion, such as including the effect of approximating Θ as constant over the filter bandwidth, primary particle polydispersity, non-uniform particle heating, and wavelength-dependent optical properties of the investigated materials' systems (soot in this case).

Acknowledgments This research was supported by the German Research Foundation within SCHU1369/20 and SCHU1369/24. We acknowledge repeated discussions with G. Smallwood (NRC, Ottawa, Canada) about experimental details related to LII signal detection.

Appendix

Additional measurement issues

Several other commonly encountered issues, in addition to the calibration errors introduced in the main text, can be encountered when interpreting LII measurements. This section therefore summarizes the observed effects and identifies strategies to avoid these anomalies.

Baseline drift

In the first 30 min of operation of the PMTs/oscilloscope, the baseline is observed to drift by up to 2% of the oscilloscope ADC voltage range before stabilizing, as the electronics thermally stabilize. Meaningful measurements and calibrations should therefore only be carried out after sufficient time is given for the equipment to warm up. The manufacturers of the PMTs used in this study recommend allowing a warm-up period of 30–60 min at similar gain supply voltages as will be used in the experiments and at anode currents of several μA [35].

Rise-time differences between channels

Differences in the rise time of different PMT channels can be caused by different cable lengths or by different photocathode materials, gain voltages, and PMT gates. The wavelength dependence of the photocathode material can only account for rise-time differences of less than 1 ns [74–76]. A more important factor is the PMT gate characteristics, which caused an observable rise-time delay between PMTs containing different photocathode materials. Figure 18 shows the PMT gate-opening characteristics for a continuous light source with a 10-ns difference in rise

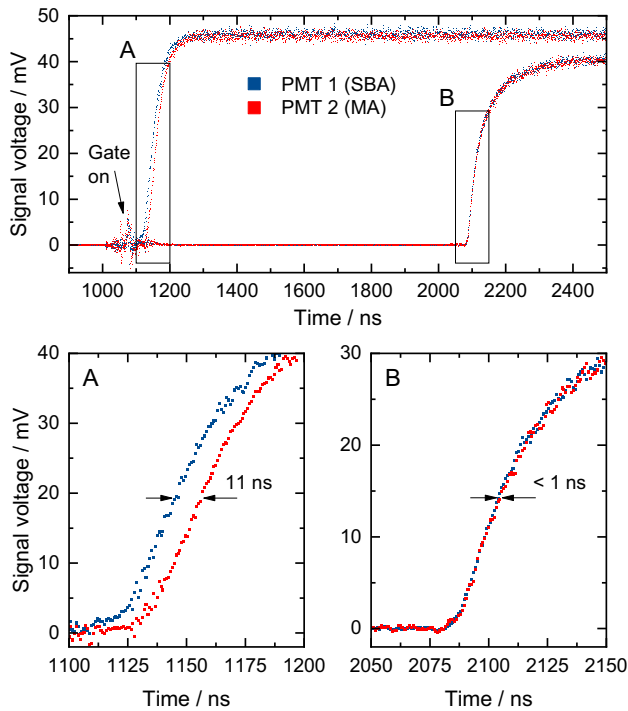


Fig. 18 Rise-time difference measured with PMTs of different photocathode materials: **a** continuously operated LED and **b** pulsed LED. For the pulsed LED, the rise-time difference was negligible (< 1 ns), while for the continuously operated LED, the gate-opening characteristics lead to a difference of 11 ns

time (A) and for a gated PMT in which the gate is opened 1 μ s before a pulsed LED, resulting in no significant difference in rise time (B). The difference in rise time could strongly influence ratio pyrometry and lead to nonphysical temperatures, particularly near the peak signal. In this scenario, temporal alignment of the LII signal peaks or the rising edge of two channels, which is a common procedure among LII practitioners, may introduce a strong bias in the calculated temperatures. Instead, it is recommended to use other signal artifacts for alignment (i.e., Q-switch noise patterns, spikes, or PMT gate opening noise) that do not coincide with the peak signal.

PMT gain stability/reproducibility

In many PMT configurations, the gain can be controlled by an external control voltage. If this voltage is not set and measured precisely, the resulting error strongly affects the gain correction calibration. Unstable power supplies for the PMTs/gain control can introduce ripple noise that propagates to the measured LII signal. Setting the gain voltages below the minimum value recommended by the manufacturer can also decrease the reproducibility of the

measurements. In cases where the gain is set too high, the noise component can increase and the measured signals can exceed the ADC voltage range of the oscilloscope. This can cause a bias for very low (i.e., baseline) and high (i.e., LII signal peak) signal levels.

Oscilloscope ADC voltage range overflow

Single-shot LII signals are usually affected by a strong noise component, and, consequently, signals must be averaged over several hundred laser shots to obtain a sufficient signal-to-noise ratio. When the LII signal peak intensity is close to the maximum of the ADC voltage range of the oscilloscope, clipping of single signal maxima can occur, biasing the average. This effect may not be obvious when examining the averaged traces.

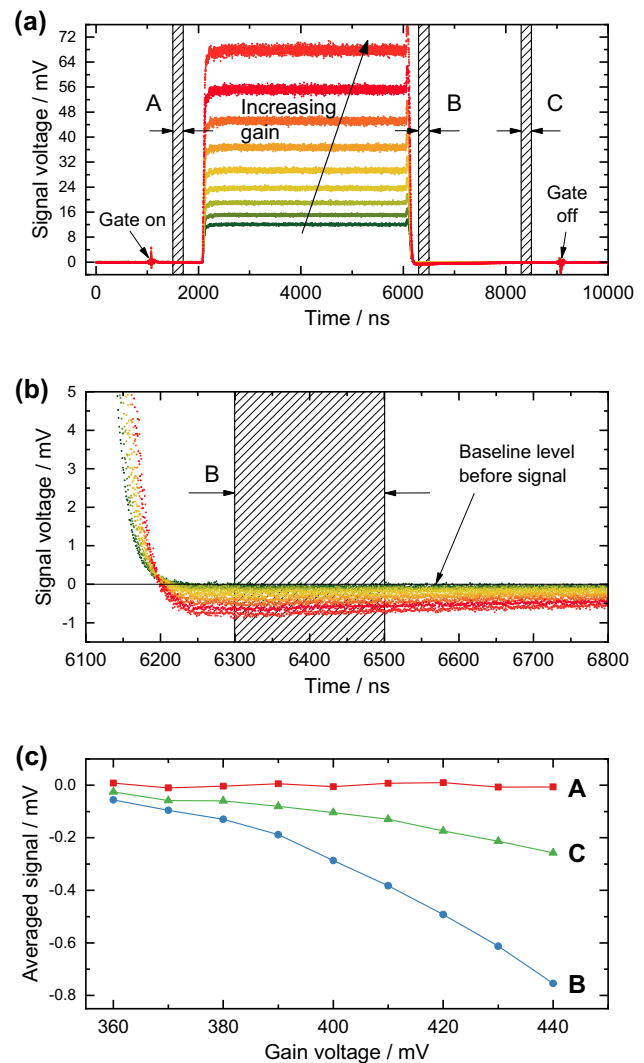


Fig. 19 PMT signals measured for pulsed LED light for increasing gain voltages (**a**, **b**). Signal sections A–C are averaged and plotted for all gain voltages in **c**

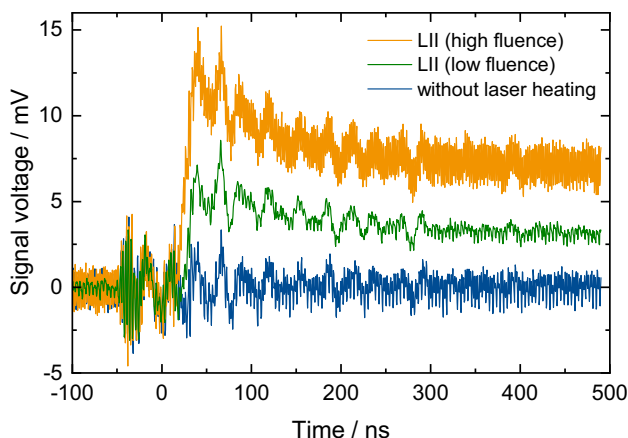


Fig. 20 Q-switch noise interfering with the measured LII signal

Signal overshooting

Signal overshooting (i.e., the signal falls below the baseline) can be caused by the charging of the capacitors in the high-voltage divider circuit of the PMT [77]. The overshooting increases with increasing gain voltage and can be detected by repeating the measurement at various gain voltages. Figure 19a shows a PMT signal measured for a pulsed LED as the gain voltage is increased. At the end of the light pulse the signal drops rapidly and the PMT signal becomes negative (b). Figure 19c shows the dependence on gain voltage for the section before the signal (A), immediately after the signal (B), and a further 2 μs later (C). The bias increases with gain voltage and can persist for several microseconds. This effect can occur for fast-decaying LII signals and significantly biases the temperature determination at later decay times.

Signal bias and artifacts

Several general measurement artifacts have been observed that are not directly connected to the LII technique, but may also lead to nonphysical results or low signal quality:

1. Signal ringing can be caused by signal reflection resulting from an impedance mismatch [78, 79].
2. Q-switch noise of the laser unit can interfere with the LII signal trace and bias the result (Fig. 20). Proper shielding of the electronics or increasing the distance between detection electronics and laser can help prevent this.
3. Crosstalk with other devices connected to the same power circuit can introduce measurement artifacts in the LII traces. Fast-switching electronic circuits (e.g., transistor circuit for shutter, pulsed light sources), for example, often appear as small spikes within the PMT signal traces.

4. Incorrect coupling of trigger/timing circuits could induce crosstalk between the oscilloscope channels. Figure 21 shows the crosstalk between the oscilloscope trigger channel and the oscilloscope signal input for two different coupling settings on the pulse/delay generator. While the spike in the beginning of the LII signal can be neglected (due to high SNR), the drift in the later part of the LII signal could bias temperature determination.
5. Low-bandwidth integrated amplifier circuits within the PMT may limit the bandwidth of the measured temporal LII signal profile. Figure 22 shows the signal response of a pulsed LED (500 nm, 3 μs FWHM) for a commercially available PMT system (PMT A) with integrated amplifier circuit (SMT MEA 1030 V8DA with Hamamatsu R7400U) and a directly coupled PMT (PMT B) from this study (Hamamatsu H11526), recorded with

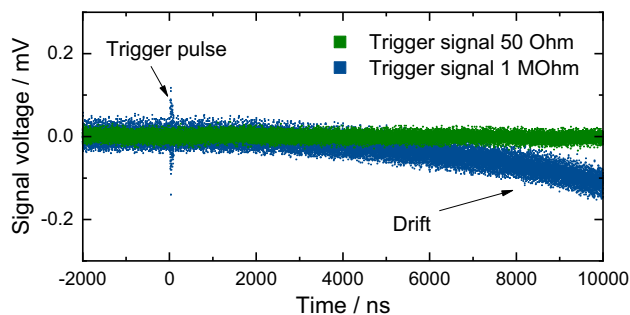


Fig. 21 Signal biased by false coupling of timing circuit (pulse/delay generator)

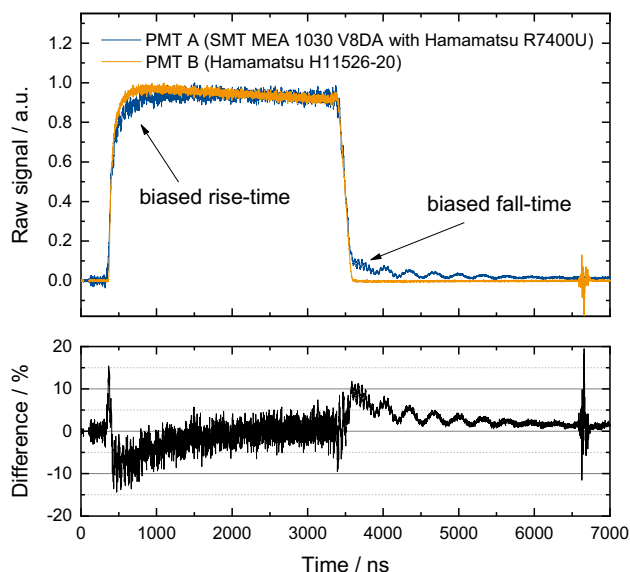


Fig. 22 Comparison of pulsed LED signal response for PMTs with (A) and without (B) integrated amplifier circuit and the difference in percent of the full ADC voltage range of the oscilloscope

the same oscilloscope. The integrated amplifier circuit influences the rise and fall characteristics, which can also bias the LII signal by limiting the temporal resolution.

References

- C. Schulz, B.F. Kock, M. Hofmann, H. Michelsen, S. Will, B. Bougie, R. Suntz, G. Smallwood, Appl. Phys. B **83**, 333 (2006)
- H.A. Michelsen, C. Schulz, G.J. Smallwood, S. Will, Prog. Energy. Combust. Sci. **51**, 2 (2015)
- T. Dreier, C. Schulz, Powder Technol. **287**, 226 (2016)
- A.V. Filippov, M.W. Markus, P. Roth, J. Aerosol. Sci. **30**, 71 (1999)
- R.L. Vander Wal, T.M. Ticich, J.R. West, Appl. Opt. **38**, 5867 (1999)
- T. Sipkens, G. Joshi, K.J. Daun, Y. Murakami, J. Heat Transf. **135**, 052401 (2013)
- T. Lehre, R. Suntz, H. Bockhorn, Proc. Combust. Inst. **30**, 2585 (2005)
- A. Eremin, E. Gurentsov, C. Schulz, J. Phys. D **41**, 055203 (2008)
- S. Maffi, F. Cignoli, C. Bellomunno, S. De Iuliis, G. Zizak, Spectrochim. Acta B **63**, 202 (2008)
- T.A. Sipkens, R. Mansmann, K.J. Daun, N. Petermann, J.T. Tiantah, M. Karttunen, H. Wiggers, T. Dreier, C. Schulz, Appl. Phys. B **116**, 623 (2014)
- T.A. Sipkens, N.R. Singh, K.J. Daun, Appl. Phys. B **123**, 14 (2017)
- J. Menser, K. Daun, T. Dreier, C. Schulz, Appl. Phys. B **122**, 277 (2016)
- F. Cignoli, S. De Iuliis, V. Manta, G. Zizak, Appl. Opt. **40**, 5370 (2001)
- D.R. Snelling, G.J. Smallwood, F. Liu, Ö.L. Gülder, W.D. Bachalo, Appl. Opt. **44**, 6773 (2005)
- C. Schulz: *Laser-Induced Incandescence: Quantitative Interpretation, Modelling, Application in Proceedings of International Bunsen Discussion Meeting and Workshop*, Duisburg, Germany, September 25–28, 2005, ISSN 1613-0073, Vol. 195, CEUR Workshop Proceedings (2005)
- R. Suntz, H. Bockhorn: *Laser-induced Incandescence: Quantitative Interpretation, Modelling, Applications*, in *Proceedings of 2nd International Discussion Meeting and Workshop*, ISSN 1613-0073, Vol. 211, CEUR Workshop Proceedings (2006)
- P. Desgroux: *Laser-induced Incandescence: Quantitative Interpretation, Modelling, Applications*, in *Proceedings of 5th International Discussion Meeting and Workshop*, ISSN 1613-0073, Vol. 865, CEUR Workshop Proceedings (2012)
- S. De Iuliis, F. Cignoli, G. Zizak, Appl. Opt. **44**, 7414 (2005)
- B. Kock, B. Tribalet, C. Schulz, P. Roth, Combust. Flame **147**, 79 (2006)
- F. Goulay, P.E. Schrader, X. López-Yglesias, H.A. Michelsen, Appl. Phys. B **112**, 287 (2013)
- R. Mansmann, T. Terheiden, P. Schmidt, J. Menser, T. Dreier, T. Endres, C. Schulz, Appl. Phys. B **124**, 69 (2018)
- K. Daun, J. Menser, R. Mansmann, S.T. Moghaddam, T. Dreier, C. Schulz, J. Quant. Spectr. Rad. Transf. **197**, 3 (2017)
- M.K. Case, D.L. Hofeldt, Aerosol. Sci. Technol. **25**, 46 (1996)
- R. Mansmann, T. Dreier, C. Schulz, Appl. Opt. **56**, 7849 (2017)
- L.J.B. Schip, B.P. Buzelatto, F.R. Batista, C.J.D. Cunha, L.C. Dias Jr., J.B.M. Novo, Química Nova **30**, 214 (2007)
- C. Knappe, J. Linden, F. Abou Nada, M. Richter, M. Alden, Rev. Sci. Instrum. **83**, 034901 (2012)
- R.L. Vander Wal, T.M. Ticich, A.B. Stephens, Appl. Phys. B **67**, 115 (1998)
- R. Mansmann, K. Thomson, G. Smallwood, T. Dreier, C. Schulz, Opt. Exp. **25**, 2413 (2017)
- B. Bougie, L.C. Ganippa, A.P. van Vliet, W.L. Meerts, N.J. Dam, J.J. ter Meulen, Proc. Combust. Inst. **31**, 685 (2007)
- M. Charwath, R. Suntz, H. Bockhorn, Appl. Phys. B **83**, 435 (2006)
- S. Schraml, S. Dankers, K. Bader, S. Will, A. Leipertz, Combust. Flame **120**, 439 (2000)
- D.R. Snelling, K.A. Thomson, G.J. Smallwood, Ö.L. Gülder, E.J. Weckman, R.A. Fraser, AIAA J. **40**, 1789 (2002)
- S. Will, S. Schraml, K. Bader, A. Leipertz, Appl. Opt. **37**, 5647 (1998)
- S.O. Flyckt, C. Marmonier, *Photonis* (Brive, France, 2002)
- T. Hakamata, Editorial Committee: (2007)
- M. Bass, *Handbook of Optics. 2. Devices, Measurements, and Properties* (McGraw-Hill, New York, 1995)
- E.H. Eberhardt, Appl. Opt. **18**, 1418 (1979)
- R.L. Vander Wal, Appl. Phys. B **96**, 601 (2009)
- C.R. Shaddix, K.C. Smyth, Combust. Flame **107**, 418 (1996)
- J. Appel, B. Jungfleisch, M. Marquardt, R. Suntz, H. Bockhorn, Symp. (Intern.) Combust. **26**, 2387 (1996)
- M.Y. Choi, K.A. Jensen, Combust. Flame **112**, 485 (1998)
- B. Axelsson, R. Collin, P.E. Bengtsson, Appl. Phys. B **72**, 367 (2001)
- J.V. Pastor, J.M. García, J.M. Pastor, J.E. Buitrago, Meas. Sci. Technol. **17**, 3279 (2006)
- R.L. Vander Wal, Z. Zhou, M.Y. Choi, Combust. Flame **105**, 462 (1996)
- D.R. Snelling, G.J. Smallwood, R.A. Sawchuk, W.S. Neill, D. Gareau, W.L. Chippior, F. Liu, Ö.L. Gülder, W.D. Bachalo, SAE Technical Paper 1999-01-3653 (1999)
- F.J. Huber, M. Altenhoff, S. Will, Rev. Sci. Instrum. **87**, 053102 (2016)
- A. Bescond, J. Yon, F.X. Ouf, C. Rozé, A. Coppalle, P. Parent, D. Ferry, C. Laffon, J. Aerosol. Sci. **101**, 118 (2016)
- H. Bladh, J. Johnsson, J. Rissler, H. Abdulhamid, N.E. Olofsson, M. Sanati, J. Pagels, P.E. Bengtsson, Appl. Phys. B **104**, 331 (2011)
- J. Yon, F.-X. Ouf, D. Hebert, J.B. Mitchell, N. Teuscher, J.-L.L. Garrec, A. Bescond, W. Baumann, D. Ourdani, T. Bizien, J. Perez, Combust. Flame **190**, 441 (2018)
- R. Sommer, A. Leipertz, Opt. Lett. **32**, 1947 (2007)
- M. Singh, J.P. Abrahamson, R.L. Vander Wal, Appl. Phys. B **124**, 130 (2018)
- F. Goulay, P.E. Schrader, H.A. Michelsen, Appl. Phys. B **100**, 655 (2010)
- G.J. Smallwood: *A Critique of Laser-Induced Incandescence for the Measurement of Soot* (PhD dissertation, Cranfield University, 2008)
- A. Eremin, E. Gurentsov, E. Mikheyeva, K. Priemchenko, Appl. Phys. B **112**, 421 (2013)
- R. Ryser, T. Gerber, T. Dreier, Combust. Flame **156**, 120 (2009)
- J. Johnsson: *Laser-Induced Incandescence for Soot Diagnostics: Theoretical Investigation and Experimental Development* (PhD dissertation, Lund University, 2012)
- E. Cenker, W.L. Roberts, Appl. Phys. B **123**, 74 (2017)
- H.H. Ku, J. Res. Natl. Bureau Stand. **70**, 263 (1966)
- T.A. Sipkens, P.J. Hadwin, S.J. Grauer, K.J. Daun, Appl. Opt. **56**, 8436 (2017)
- C.F. Bohren, D.R. Huffman, *Absorption and Scattering of Light by Small Particles* (Wiley, Oxford, 2008)
- T.A. Sipkens, J. Menser, R. Mansmann, C. Schulz, K.J. Daun: Appl. Phys. B (2019)

62. P.J. Hadwin, T.A. Sipkens, K.A. Thomson, F. Liu, K.J. Daun, *Appl. Phys. B* **122**, 1 (2016)
63. P.J. Hadwin, T.A. Sipkens, K.A. Thomson, F. Liu, K.J. Daun, *Appl. Phys. B* **123**, 114 (2017)
64. U. von Toussaint, *Rev. Mod. Phys.* **83**, 943 (2011)
65. F. Liu, D.R. Snelling, K.A. Thomson, G.J. Smallwood, *Appl. Phys. B* **96**, 623 (2009)
66. E.S. Fry, J. Musser, G.W. Kattawar, P.-W. Zhai, *Appl. Opt.* **45**, 9053 (2006)
67. Ö.L. Gülder, D.R. Snelling, R.A. Sawchuk, *Symp. (Intern.) Combust.* **26**, 2351 (1996)
68. E. Nordström, N.-E. Olofsson, J. Simonsson, J. Johnsson, H. Bladh, P.-E. Bengtsson, *Proc. Combust. Inst.* **35**, 3707 (2015)
69. H. Bladh, J. Johnsson, P.E. Bengtsson, *Appl. Phys. B* **96**, 645 (2009)
70. G. Cléon, T. Amodeo, A. Faccinetto, P. Desgroux, *Appl. Phys. B* **104**, 297 (2011)
71. F. Liu, B.J. Stagg, D.R. Snelling, G.J. Smallwood, *Int. J. Heat Mass Transf.* **49**, 777 (2006)
72. F. Liu, M. Yang, F.A. Hill, D.R. Snelling, G.J. Smallwood, *Appl. Phys. B* **83**, 383 (2006)
73. F. Liu, S. Rogak, D.R. Snelling, M. Saffaripour, K.A. Thomson, G.J. Smallwood, *Appl. Phys. B* **122**, 286 (2016)
74. R.K. Bauer, A. Balter, *Opt. Commun.* **28**, 91 (1979)
75. P. Wahl, J.C. Auchet, B. Donzel, *Rev. Sci. Instrum.* **45**, 28 (1974)
76. B. Sipp, J.A. Miehe, R. Lopez-Delgado, *Opt. Commun.* **16**, 202 (1976)
77. F.-J. Luo, Y.-K. Heng, Z.-M. Wang, P.-L. Wang, Z.-H. Qin, M.-H. Xu, D.-H. Liao, H.-Q. Zhang, Y.-B. Huang, X.-C. Lei, S. Qian, S.-L. Liu, Y.-B. Chen, Y.-F. Wang, *Chin. Phys. C* **40**, 096002 (2016)
78. B.H. Candy, *Rev. Sci. Instrum.* **56**, 183 (1985)
79. C. Knappe, F. Abou Nada, M. Richter, M. Alden, *Rev. Sci. Instrum.* **83**, 094901 (2012)

Publisher's Note Springer Nature remains neutral with regard to jurisdictional claims in published maps and institutional affiliations.